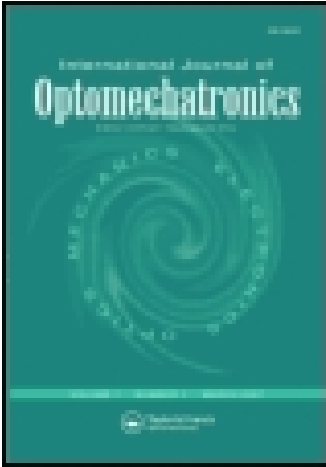


This article was downloaded by: [Universidad de Sevilla]

On: 18 November 2014, At: 03:29

Publisher: Taylor & Francis

Informa Ltd Registered in England and Wales Registered Number: 1072954 Registered office: Mortimer House, 37-41 Mortimer Street, London W1T 3JH, UK



International Journal of Optomechatronics

Publication details, including instructions for authors and subscription information:

<http://www.tandfonline.com/loi/uopt20>

A Flexible Experimental System for Complex Microassembly under Microscale Force and Vision-Based Control

Hui Xie ^a, Weibin Rong ^a & Lining Sun ^a

^a Robotics Institute, Harbin Institute of Technology, Harbin, People's Republic of China

Published online: 30 Mar 2007.

To cite this article: Hui Xie, Weibin Rong & Lining Sun (2007) A Flexible Experimental System for Complex Microassembly under Microscale Force and Vision-Based Control, International Journal of Optomechatronics, 1:1, 81-102, DOI: [10.1080/15599610701232648](https://doi.org/10.1080/15599610701232648)

To link to this article: <http://dx.doi.org/10.1080/15599610701232648>

PLEASE SCROLL DOWN FOR ARTICLE

Taylor & Francis makes every effort to ensure the accuracy of all the information (the "Content") contained in the publications on our platform. However, Taylor & Francis, our agents, and our licensors make no representations or warranties whatsoever as to the accuracy, completeness, or suitability for any purpose of the Content. Any opinions and views expressed in this publication are the opinions and views of the authors, and are not the views of or endorsed by Taylor & Francis. The accuracy of the Content should not be relied upon and should be independently verified with primary sources of information. Taylor and Francis shall not be liable for any losses, actions, claims, proceedings, demands, costs, expenses, damages, and other liabilities whatsoever or howsoever caused arising directly or indirectly in connection with, in relation to or arising out of the use of the Content.

This article may be used for research, teaching, and private study purposes. Any substantial or systematic reproduction, redistribution, reselling, loan, sub-licensing, systematic supply, or distribution in any form to anyone is expressly forbidden. Terms & Conditions of access and use can be found at <http://www.tandfonline.com/page/terms-and-conditions>

A FLEXIBLE EXPERIMENTAL SYSTEM FOR COMPLEX MICROASSEMBLY UNDER MICROSCALE FORCE AND VISION-BASED CONTROL

Hui Xie, Weibin Rong, and Lining Sun

Robotics Institute, Harbin Institute of Technology, Harbin,
People's Republic of China

A flexible experimental system developed for efficient and stable complex microassembly is presented. The system consists of a set of modules that can adapt their shape and function to various assembly tasks. Due to the basic limitations of microscopic vision, a wavelet-based focus measure to obtain both high precision and robust autofocus, a control scheme with a modified Smith predictor to decrease the inherent time delay of vision systems, and microscopic vision/force integration to control the assembly tasks are proposed. A smart 3-D PVDF (Polyvinylidene Fluoride) force sensor is employed to sense the interactive force. Analysis and microassembly of three planetary gears demonstrate that this system has high flexibility.

1. INTRODUCTION

An important trend in the design and development of microassembly systems is their versatility, flexibility, and robustness to achieve small and medium sized batches assembled in an economical way. Different microassembly systems have been reported (Vikramaditya and Nelson 1997; Eberhardt et al. 1997; Woern et al. 2000) including the microassembly of micro-mechanic, opto-electronic, and micro-fluidic devices. Due to the characteristics of these microparts, corresponding manipulation methods, grippers, fixtures, and positioning systems have been developed (Santa et al. 1999; Lee and Kang 2003; Ralis et al. 2000). The microassembly task has many demands, including accuracy, workspace, and manipulation capacity. It is difficult to design a microassembly system with a fixed structure that is versatile and accurate to meet many task requirements of microassembly. However, a flexible microassembly system can offer adaptability without incurring a higher cost, while at the same time offering new functionalities for various microassembly tasks. There are a growing number of flexible systems that have been developed (Maeda et al. 2003; Sugi et al. 2003). These systems aim at many desirable characteristics including versatility, flexibility, and robustness. An economical reconfigurable assembly system with low cost sensors and actuators was designed to handle fiber-optic and micro-optical components (Popa et al. 2002). Relations between system adaptability and flexibility were presented, and the method to

Address correspondence to Hui Xie, Robotics Institute, Harbin Institute of Technology, Harbin 150080, People's Republic of China. E-mail: xiehui@hit.edu.cn

achieve task-oriented configuration of reconfigurable robotic systems was developed (Bi et al. 2003).

Optomechatronic integration is an essential part of the development of flexible microassembly systems due to the importance of microscope optics to microassembly (Yang et al. 2005). In our system, microscopic computer vision plays a fundamental role in the microassembly task, and it is employed along with a smart 3-D PVDF force sensor for the microassembly tasks.

This article presents the flexible system design for complex microassembly and is organized as follows. Section 2 presents the hardware architecture of the flexible system in detail. A new wavelet-based focus measure and a control scheme with a modified Smith predictor (MSP) to eliminate the inherent time delay of visual servoing are introduced in Section 3. Microscopic vision/force integration techniques are introduced in Section 4. Microassembly of planetary gears is presented in Section 5. Conclusions are discussed in Section 6.

2. SYSTEM ARCHITECTURE AND OPERATION

2.1. Microassembly Task Descriptions

Microassembly systems with high precision, flexibility, robustness, and dexterity are essential to micro electronic mechanical system (MEMS) and micro-optical electronic mechanical system (MOEMS) fabrication. Our research aims at building a microassembly system that can achieve a set of MEMS and MOEMS assembly tasks. Application examples include silicon pressure sensor bonding, miniaturized gear system assembly, and fiber-optic component handling (Sun et al. 2005). In this study, assembly of a miniaturized gear system is introduced. Figure 1 shows the miniaturized gear system, with an outer diameter of less than 2.0 mm. The miniaturized gear system consists of nine components with a module of 0.03, including three planetary gears, a sun gear, a fixed annular wheel, an output, internal toothed wheel, a frame base, an output, and an input shaft. In our experiments, the task is to assemble three planetary gears into the base frame under the navigation of vision and force.

The requirements of the assembly are complex and have to be taken into consideration during the design and fabrication process. In our experiment, the MEMS

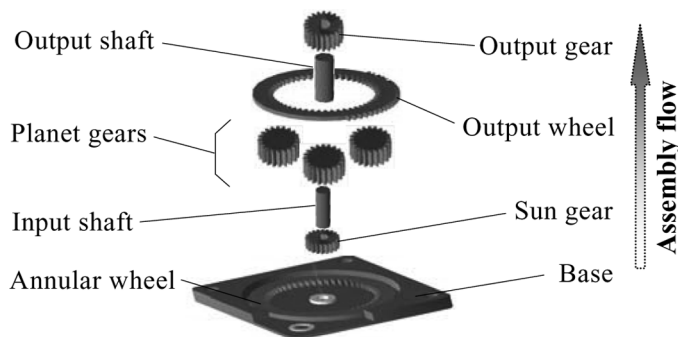


Figure 1. Microassembly of the miniaturized gear system.

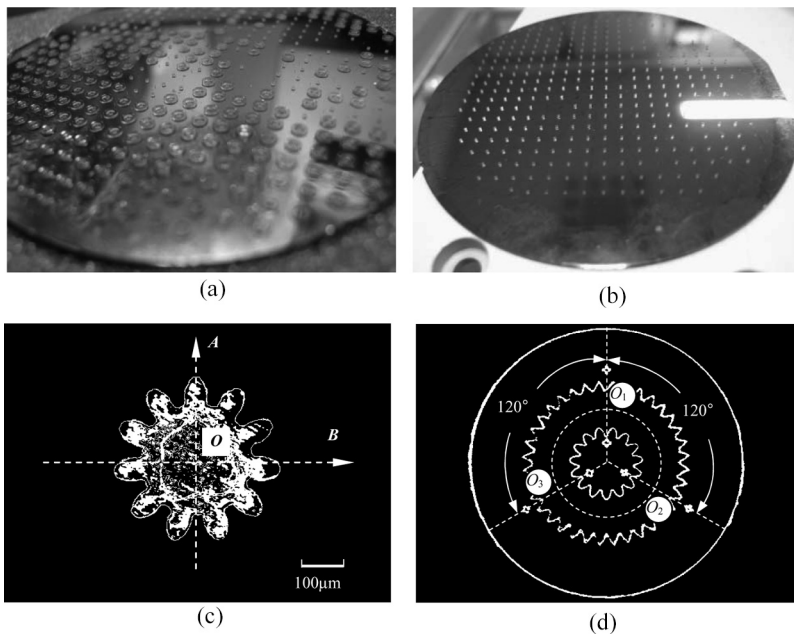


Figure 2. Illustrations of miniaturized gears: (a) the array of the internal toothed wheel and sun gears on a wafer; (b) the array of planetary gears on a wafer; (c) the binary image of the planetary gear, where O is the centroid of planetary gear; and (d) the binary image of the base frame with marks onto the surface of the sun gear and annular wheel, where O_1 , O_2 , and O_3 are the midpoints of each two radial marks.

gears, fabricated by LIGA technology, are arrayed on the wafer substrate. As Figures 2a and 2b show, the planetary gears and base frames are fabricated onto the substrate with the same arrangement. The space between each of the four microparts is $2.5 \text{ mm} \times 2.5 \text{ mm}$, which is enough for the successful grasping without interference.

2.2. Microassembly Process Flow

Compared with previous microassembly work, such as manipulating a glass fiber into a V-groove (Zhou et al. 1998) and the assembly of opto-electrical components (Kim et al. 2003), the assembly of a miniaturized gear system is more complex and challenging. As Figure 1 shows, the assembly flow is “from bottom to top.” Microparts like the shaft and the housing components are manufactured by precision engineering methods and have chamfers, so the assembly of these components is relatively easy. Therefore, the following explanations will concentrate on the most crucial assembly tasks of the planetary gears. The whole assembly process is performed as follows (Xie et al. 2005).

2.2.1. Grasping and Transferring After the system is initialized, a planetary gear is picked up and then moved to the desired assembly position under the navigation of microscopic visual servoing.

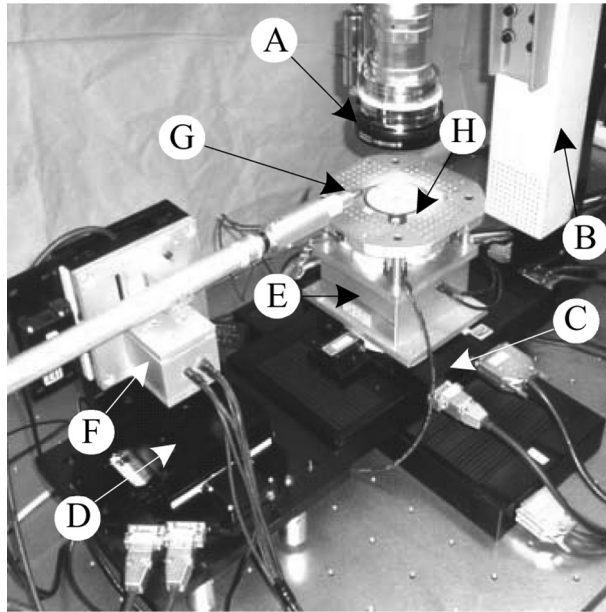


Figure 3. The flexible microassembly system: A: the optical microscope and the imaging system; B: the autofocusing machine; C: the 3-DOF coarse motion stage (positioning); D: the 3-DOF coarse motion stage (micromanipulator); E: the 2-DOF fine motion stage (positioning); F: the 3-DOF fine motion stage (micromanipulator); G: the gripper; and H: the vacuum fixture.

2.2.2. Searching A fuzzy PID controller is used to control the contact force of the z axis and a logic strategy is used to search the engaging state between the planetary gears and the base frame by the force feedback on the X - Y plane.

2.2.3. Inserting A movement named “tolerance compensation movement” is used to overcome the blocking circles during the inserting step and safely achieve non-destructive assembly.

2.3. Detailed System Architecture

The flexible experimental microassembly system shown in Figure 3 consists of the following functional units.

2.3.1. Microscope and Imaging System This unit provides image capturing. In the microassembly system, one microscope (HIROX MX-5030R, $1\times -6\times$) and imaging system is used to obtain a top view of the assembly parts. The magnification is adjustable to view various sizes of microparts. Images are captured using a PCI frame card (Da-Heng CG400). For high resolution motion on the optical axis of the microscope, a linear motor driven motion stage that travels 7.5 mm and has a step resolution of $0.1\ \mu\text{m}$ is used to provide motion control of autofocusing tasks.

2.3.2. Coarse Positioning Stages The coarse positioning system used for part feeding and other tasks requires a large workspace. The coarse positioning

Table 1. Specifications of coarse positioning stages

Classification	Specifications		
	Range (mm)	Resolution (μm)	accuracy (μm)
Positioning stage			
x	150	1.8	6
y	100	1.8	6
θ_z	no limits	0.005°	0.02°
Micromanipulator			
x	50	1.0	3
y	50	1.0	3
z	50	1.0	3

stages of this system are comprised of five linear positioning stages and one rotary stage actuated by ultrasonic motors. All the ultrasonic motors are controlled by a parallel control system, and the feedback data is generated by a precise grating encoder. Parameter specifications of each stage are shown in Table 1.

2.3.3. Fine Positioning Stages The fine positioning system ensures the given accuracy demands of joining and assembly processes. As a novel actuator, compared with other actuators, piezoelectric ceramics have many impressive advantages, e.g., high resolution, rapid response, large force per volume, and litter caloric (Zhai et al. 2000). Therefore, piezoelectric ceramics are the perfect actuator of the micropositioning stage. In general, an integrated closed loop system used for micropositioning is composed of an integrated actuator, an actuator electrical source, a position sensor, and a controller and zoom mechanics these five components. A set of piezo-actuated fine positioning stages have been developed in our lab (Qu et al. 2002; Liu et al. 2002). Figures 4a and 4b show the structure of fine stages. Figures 4c and 4d show a 2-DOF linear fine positioning stage and a 5-DOF fine positioning stage. The corresponding parameter specifications are described in Table 2.

2.3.4. Micromanipulator This unit provides high precision motion control and stable manipulation for grasping, transferring, and assembling microparts. The unit consists of a 3-DOF coarse motion stage, a 3-DOF fine motion stage, a 3-D PVDF force sensor, and a microgripper. The specifications of coarse and fine motion stage units are described in Tables 1 and 2. As Figures 4e and 4f show, a piezo-actuated gripper with EDM machined clamping jaws is used to manipulate gears of different sizes (from 400 μm to 2000 μm in diameter). The opening distance of the jaws is about 200 μm , which is controlled by our modular DSP-based controller. Figures 4g and 4h show the 3-D PVDF force sensor, which has a resolution of less than 0.24 mN on each axis. It is developed to measure the contact and assembly force during the manipulation process, to protect the sensitive components from destruction, and to search the engaging states. Parameters of the PVDF force sensor are shown in Table 3.

2.3.5. Auxiliary Systems These units include a vacuum fixture for wafer fixing, a gas supply station, environment control, vibration isolation, etc.

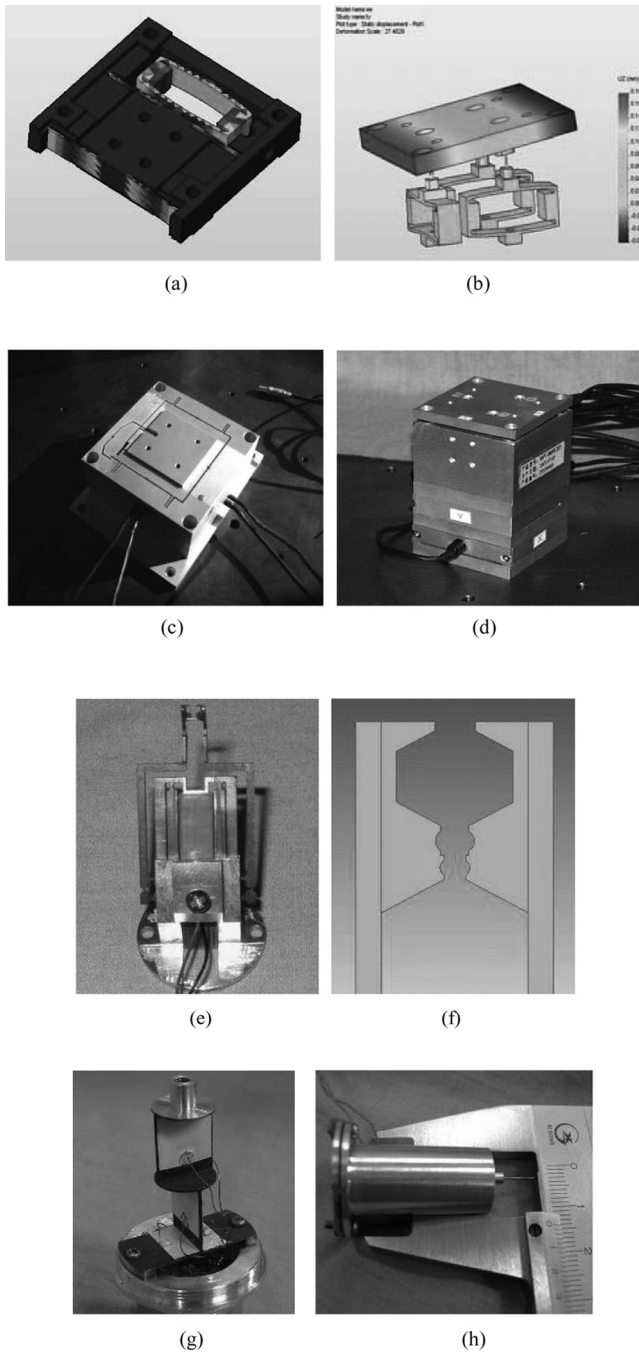


Figure 4. Components of the flexible microassembly system: (a) the structure of 1-DOF Pizeo-actuated linear positioning stage; (b) the structure of 3-DOF Pizeo-actuated parallel stage; (c) the 2-DOF Pizeo-actuated fine positioning stage; (d) the 5-DOF Pizeo-actuated fine positioning stage; (e) the Pizeo-actuated microgripper; (f) EDM machined clamping jaws; (g) the structure of the 3-D PVDF force sensor; and (h) the packaged force sensor.

Table 2. Specifications of fine positioning stages

Classification	Specifications		
	Range (μm)	Resolution (nm)	Accuracy (nm)
2-DOF linear stage			
x	100	30	100
y	100	30	100
z	50	20	50
3-DOF parallel stage			
θ_x	0.06°	0.00006°	0.0002°
θ_y	0.06°	0.00006°	0.0002°

3. MICROSCOPIC VISION

3.1. Basic Properties of Microscopic Optics

Optomechatronic integration is considered at a physical implementation level and an algorithm level. Mechatronic design for physical implementation has been introduced in Section 2. This section focuses on the algorithm design for microscope visual servoing. A high resolution microscope is required for high precision assembly. High resolution optical lenses have large numerical apertures and high magnifications, which have the basic properties of small field-of-view, limited depth-of-field, and small working distance (Vikramaditya 2001).

3.2. A New Wavelet-based Focus Measure

Due to the property of limited depth-of-field, each microscopy image will show certain parts of the specimen in and out of focus. Therefore, autofocus is a fundamental technology for automated micromanipulation, and its essential technique is the focus measure. A variety of spatial focus measures have been proposed (Groen et al. 1985; Firestone et al. 1991; Subbarao et al. 1993). These three focus measures, namely normalized variance (M_V), entropy (M_E), and energy laplace (M_L), have been reported as the classic and popular focus measures. Among these measures, energy laplace and normalized variance have been reported to be the most effective (Subbarao and Tyan 1998; Sun et al. 2004). Recently, two wavelet-based high frequency focus measures have been constructed (Yang and Bradley 2003) in which the squared one (M_2) provides better focus performance than previous spatial domain operators, and the absolute one provides performance equivalent to that of the best spatial domain operators. In this section, a new focus measure M_W based

Table 3. Calibration results of the 3-D PVDF force sensor

Dimension	Sensitivity (mv/mN)	Range (mN)	Resolution (mN)
X	94.8	± 50	0.15
Y	92.9	± 50	0.15
Z	62.2	± 80	0.24

on wavelet transform is constructed, which provides significantly better performance and robustness than previous ones.

3.2.1. Definition The new focus measure is based on the discrete wavelet transform (DWT). The image blurring is caused by convolution of the origin image $g(x, y)$ with the point-spread function (PSF), which has a character of an unknown low-pass filter. So it is easy to understand intuitively that the DWT has this property: blurring (or defocusing) in the image decreases the energy in the high-pass bands and simultaneously increases the energy in the low-pass band. When focusing the image, the high frequency coefficients increase and simultaneously coefficients of low frequency decrease. It can be considered that orthogonal DWT preserves the image energy. So we propose a square wavelet-based focus measure, which is defined as

$$M_w = \frac{M_H^2}{M_L^2} \quad (1)$$

where M_H^2 and M_L^2 are defined as follows

$$M_H^2 = \sum_{l=1}^K \left[\sum_{(x,y) \in S_{LHI}} W_{LHI}^2(x, y) + \sum_{(x,y) \in S_{HLI}} W_{HLI}^2(x, y) + \sum_{(x,y) \in S_{HHI}} W_{HHI}^2(x, y) \right] \quad (2)$$

$$M_L^2 = \sum_{(x,y) \in S_{LL}} W_{LLK}^2(x, y) \quad (3)$$

where S denotes an operator window whose corresponding operator windows in level- l LHI , HLI and HHI subbands are denoted S_{LHI} , S_{HLI} , S_{HHI} , respectively. The high frequency coefficients in these sub-bands are W_{LHI} , W_{HLI} , and W_{HHI} . The K^{th} level low frequency coefficient is W_{LLK} .

The selection of wavelet bases and performance comparisons of M_w with normalized variance, entropy, energy laplace, and wavelet-based squared high frequency use five image samples obtained under a bright field with $5\times$, $25\times$, $50\times$, $100\times$ and $200\times$ magnifications, as shown in Figure 5. The same image sequences are obtained in the same step on the optical axis of the microscope. For example, the low NA image sequence under $5\times$ magnification was obtained in $40\mu\text{m}$ steps. Each image sequence consists of 49 images, in which image no. 25 is determined to be satisfactorily in-focus by human observation.

3.2.2. Performance Metrics In order to make valid evaluations, five metrics have been used for a systematic evaluation of several focus measures (Santos et al. 1997). In our experiments, the focus measures were evaluated using the following five performance metrics: accuracy, resolution, number of false maxima, width, and noise level. The focus measures were ranked according to individual criteria as well as overall score.

The metrics Accuracy and Resolution are defined as

$$\text{Accuracy} = |Z_{+e} - Z_{-e}| \quad (4)$$

$$\text{Resolution} = \sigma = \frac{1}{\|M\|} \left[\sum_{x \in S} (z - Z_f)^2 M^2(z) \right]^{1/2} \quad (5)$$

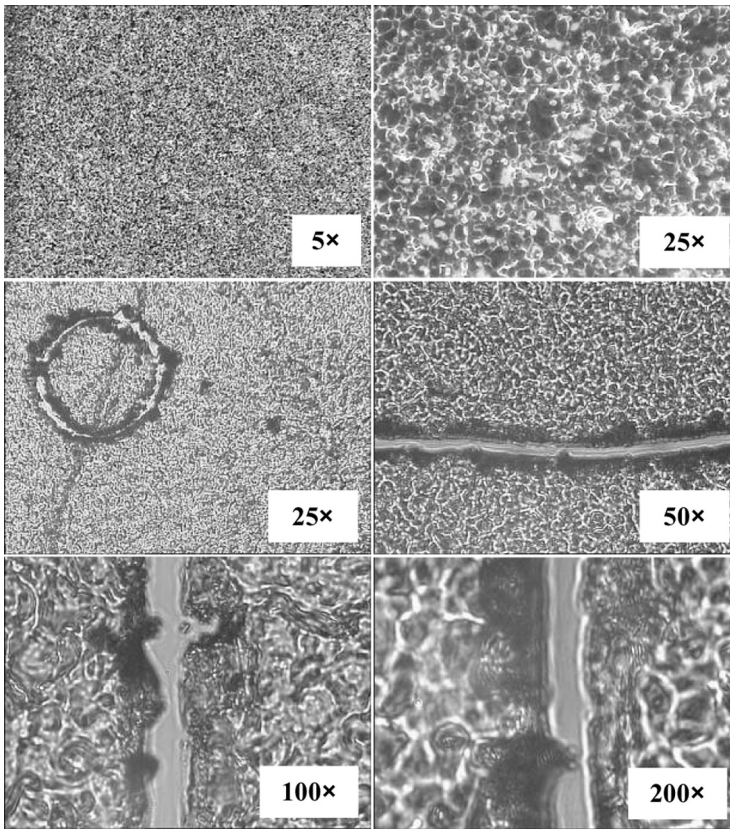


Figure 5. Images of samples with various magnifications.

where Z_{-e} and Z_{+e} are the detected neighborhood of in-focus position. The error allowance e can be chosen by a specified number, in our experiments $e = 2.0\%$. $\|M\| = \|M\|_2$, which is derived from the standard definition of resolution used in the statement of the Heisenberg uncertain principle (Mallat 1999), and a similar definition is used in (Yang and Nelson 2003). This metric can characterize the distribution of the profile of the focus measure and simultaneously characterizes how well out-of-focus features are suppressed.

3.2.3. Selection of Wavelet Bases Wavelet bases, including Daubechies, Coiflets, and Symlets with vanishing moments of 4, 6, and 8 and decomposition depths from 1 to 4, are used to compare the performance of various wavelet bases. Experimental results show that the Daubechies with 6 vanishing moments under 3-decomposition depth is a good compromise for common microscopy images.

3.2.4. Performance Comparisons By comparing experimental results, one can see that accuracy, resolution, number of false maxima, width, and noise level are almost consistently improved for all the focus measure, along with the increasing of the magnification. In terms of rankings of all the metrics and overall score, magnification differences make little change of focus measures. Table 4 shows the

Table 4. Ranking of focus measures using noise-free image sequences

Metrics	Accuracy	Resolution	False max.	Width	Noise level	Overall score
M_2	1.41 (3)	1.77 (4)	3.97 (5)	6.82 (4)	1.94 (4)	1.38 (4)
M_W	1.14 (1)	1.23 (1)	0 (1)	4.12 (2)	0.20 (3)	0.50 (1)
M_E	19.48 (5)	2.62 (5)	0 (1)	32.34 (5)	0.14 (2)	1.79 (5)
M_V	2.24 (4)	1.47 (3)	0 (1)	6.46 (3)	0.12 (1)	0.61 (2)
M_L	1.42 (2)	1.34 (2)	0 (1)	3.94 (1)	3.02 (5)	1.13 (3)

performance and rank of five focus measures using noise-free images according to individual metric distances and overall score. Each entry is based on eight image sequences and averaged. By comparing the overall scores, the proposed focus measure M_W is found to provide the best overall performance.

3.2.5. Robustness Comparisons of Focus Measures In order to evaluate the robustness of the focus measures, each metric distance is computed based on noisy image sequences. In our experiments, each of the images is corrupted by Gaussian white noise with standard deviations (STD) 5, 15, 25, and 35, respectively. In this way, 32 series of 49 noisy images each, are used to compare robustness of the five focus measures. Table 5 shows the performance and ranks of five focus measures using noisy images according to individual metric distances and the overall score. Each entry in this table is based on 32 image sequences and averaged. One can see that the proposed focus measure provides the best overall performance in robustness evaluation.

3.3. Visual Servoing with MSP

Due to the time-consuming image acquisition, transfer, and processing, the visual servoing has an inherent time delay, which impedes the system performance. Previously, the most common method is to decrease the primary gains to increase damping, thus making the system more robust in the presence of delays. However, the resultant response of the system will be lowered, leading to a sluggish overall performance. In our research, a control scheme with a similar structure to the Smith predictor, called modified Smith predictor, is employed to eliminate the vision delay.

3.3.1. Set-up of the Visual Servoing Controller The conventional Smith predictor was developed for dealing with dead-time problems common to industrial process where feedback is continuous; that is, the system is a continuous one. However, the system with a visual servoing is discrete due to the long image

Table 5. Ranking of focus measures using noisy image sequences

Measures	Accuracy	Resolution	False max.	Width	Overall score
M_2	2.56 (2)	5.95 (4)	9.21 (5)	35.72 (4)	1.59 (5)
M_W	1.62 (1)	3.89 (2)	1.69 (3)	4.67 (1)	0.68 (1)
M_E	24.97 (5)	6.07 (5)	0.13 (1)	48.00 (5)	1.73 (4)
M_V	3.21 (4)	3.52 (1)	1.02 (2)	7.53 (2)	0.82 (2)
M_L	2.79 (3)	5.71 (3)	7.02 (4)	28.23 (3)	1.17 (3)

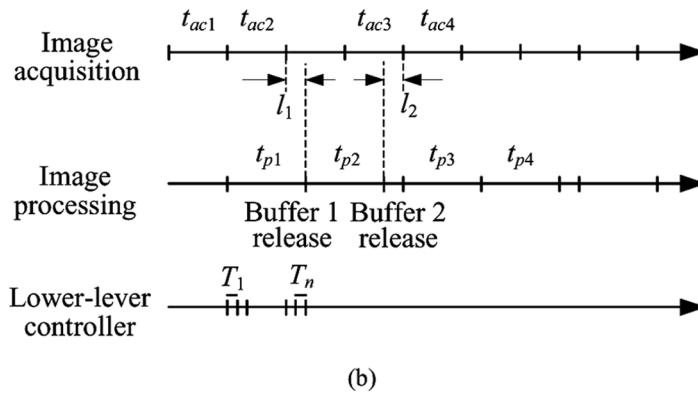
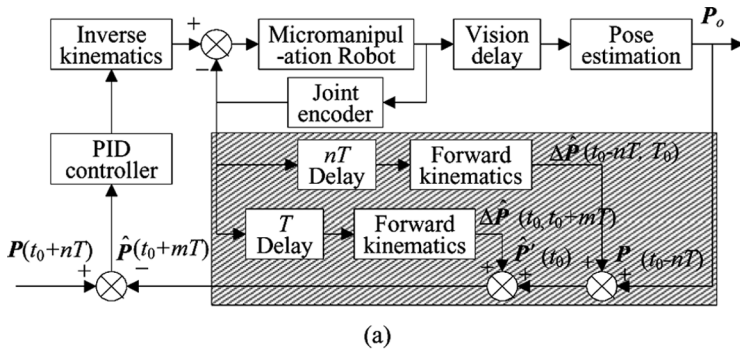


Figure 6. Illustrations of the visual servoing system: (a) the visual servoing architecture with MSP; and (b) the timing model.

capturing and processing time of each captured frame. Furthermore, the delay is variable, depending on the complexity of a given image. Consequently, the original Smith predictor is not suited for visual feedback, and some modifications are proposed to overcome these limitations.

In the case of a discrete visual feedback, the feedback is available only every n step and the system error can only be modified every n step. Therefore, a modified Smith predictor can store the correction factor until the next visual feedback becomes available. The MSP for the discrete visual servoing system is illustrated in Figure 6a (shadow area). Here, t_0 is the time at which visual feedback becomes available; the delay nT of visual predictor loop is equal to the vision delay; $P(t_0 - nT)$ is an estimate of output signal at time $t_0 - nT$ by visual feedback; $\Delta\hat{P}(t_0 - nT, t_0)$ and $\hat{P}(t_0 - nT)$ are estimates of the displacement from $t_0 - nT$ to t_0 ; and the actual position of system at time $t_0 - nT$ calculated by the joint feedback, respectively. $\Delta\hat{P}(t_0, t_0 + mT)$ is an estimate of the displacement from time t_0 to $t_0 + mT$; $\hat{P}(t_0)$ is calculated from the actual position at time $t_0 - nT$, which is known at time t_0 ; and $\hat{P}(t_0 + mT)$ is the estimation of the current position at time $t_0 + mT$ ($m \leq n$). Due to the time delay, a visual feedback cycle usually involves several joint feed-back cycles. Therefore the robot's current position $P(t)$ estimated by the visual feedback only become available at time $t + nT$, where t is the controller cycle time. Therefore $P(t)$ is not the robot's current

position but the past one. A better control scheme should be used to obtain a better estimation $\widehat{\mathbf{P}}'(t)$ of the position at time t based on the visual feedback and the joint feedback $\widehat{\mathbf{P}}(t)$. The conventional Smith predictor is suitable for the continuous system, not a discrete one.

$$\widehat{\mathbf{P}}'(t_0) = \mathbf{P}(t_0 - nT) + \Delta\widehat{\mathbf{P}}(t_0 - nT, t_0) \quad (6)$$

$$\widehat{\mathbf{P}}'(t_0 + mT) = \widehat{\mathbf{P}}'(t_0) + \Delta\widehat{\mathbf{P}}(t_0, t_0 + mT) \quad (7)$$

where $\Delta\widehat{\mathbf{P}}(t_0 - nT, t_0)$ and $\Delta\widehat{\mathbf{P}}(t_0, t_0 + mT)$ are defined as

$$\Delta\widehat{\mathbf{P}}(t_0 - nT, t_0) = nT \cdot \dot{\widehat{\mathbf{P}}}(t_0 - nT) \quad (8)$$

$$\Delta\widehat{\mathbf{P}}(t_0, t_0 + mT) = \frac{mT}{n} \cdot (\widehat{\mathbf{P}}(t_0 - nT) - \widehat{\mathbf{P}}(t_0 - 2nT)) \quad (9)$$

where $\dot{\widehat{\mathbf{P}}}(t_0 - nT)$ denotes the predicted velocity at time, t_0 , based on the current measurement at delayed time $t_0 - nT$.

$$\dot{\widehat{\mathbf{P}}}(t_0 - nT) = \dot{\widehat{\mathbf{P}}}(t_0 - 2nT) + (\Delta\widehat{\mathbf{P}}(t_0 - nT, t_0) - \Delta\widehat{\mathbf{P}}(t_0 - 2nT, t_0 - nT))/nT \quad (10)$$

From the equations mentioned above, the estimated position $\widehat{\mathbf{P}}'(t_0 + mT)$ at the time $t_0 + mT$ can be described as

$$\widehat{\mathbf{P}}'(t_0 + mT) = \widehat{\mathbf{P}}'(t_0) + \frac{mT}{n} (\widehat{\mathbf{P}}(t_0 - nT) - \widehat{\mathbf{P}}(t_0 - 2nT)) \quad (11)$$

Hence, the required error signal $e(t_0 + nT)$ can be defined

$$e(t_0 + nT) = \mathbf{P}(t_0 + nT) - \widehat{\mathbf{P}}'(t_0 + mT) \quad (12)$$

The error signal is then fed into a PID digital controller

$$u_i(n) = K_P \left(e(n) + \frac{k_i}{T_I} \sum_{i=0}^n e_i T + T_D \frac{e(k) - e(k-1)}{T} \right) \quad (13)$$

where K_P , T_D , and T_I are the gains of the PID Controller. T is the discrete lower controller sampling time. To avoid the integral windup effect, an anti-windup controller is used:

$$k_i = \begin{cases} 0 & \text{when } |e(n)| > \varepsilon, \text{ acts as a PD controller} \\ 1 & \text{when } |e(n)| \leq \varepsilon, \text{ acts as a PID controller} \end{cases} \quad (14)$$

where ε is a threshold of the error that can be obtained by experiments. Rapid response will be obtained when the controller acts as a PD controller, and the steady state error will be eliminated while the controller acts as a PID controller. The PID

parameters will be determined through the normal heuristic tuning procedure using the root mean square of the tracking errors as the performance index.

3.3.2. Time Modeling The vision delay consists of image acquisition, image processing, and signal transfer time. As a result, one loop takes, at the minimum, about 60 ms to much more than one second at the maximum. The lower-lever control loop takes $1/n$ time of vision delay, which is employed as a computed torque controller. Note that the vision delay is not a constant, which can vary from image to image. To set up an exact model of the MSP controller, a time model should be introduced.

The vision delay varies from different types of vision processing structures. It has four configurations of on-the-fly, serial, parallel, and pipeline processing (Markus 2000). A parallel configuration is employed in our system, where two input buffers are used to store the image. In this case, the second image buffer is being filled while the data in the first image is being processed. Therefore, the delay of one visual feedback cycle is mainly composed of image processing time.

A continuous generic timing model to describe asynchronous vision-based control systems for the control of industrial manipulator is introduced (Liu et al. 2004). Figure 6b illustrates the timing model for the visual control loop and the lower-lever control loop in our study. This model is used to establish the closed-loop cycle and quantify the processing time of the system, which can be expressed as $t_p = nT$. Note that the storage lag l_1 is the time between the end of storage time of buffer 2 and the start of processing time. Similarly, the processing lag l_2 is the time between the end of processing time and the start of storage time of buffer 2.

This section gives representative experiment results pertaining to the use of modified Smith predictor control scheme for visual servoing control. Target-tracking and disturbance rejection capabilities will be studied in using a modified Smith predictor control scheme compared with a normal single visual feedback control loop. The visual feedback loop operates at 10 Hz while the robot servoing rate is 500 Hz. A fixed time delay of 100 ms of visual servoing is assumed.

To validate the closed-loop response and the capability of the disturbance rejection, a miniaturized gear is placed on the focus plane for a point to point response experiment and to keep the gear in the center of the field-of-view with the external disturbances. Due to the poor depth of the microscope focus, the planar tacking is also executed on the focus plane of the microscope. To have a valid comparison of the tracking performance, both of the control systems have the same elemental parameter. The field-of-view of microscope is about 1.4×1.1 mm with a multiple of 4.5.

The closed-loop responses and disturbance rejection results with a single PID controller and with a modified Smith predictor are presented in Figure 7, respectively. In the case of the same system gain, the results show that the visual servoing control system with MSP in comparison to a single PID controller provides more robustness and disturbance rejection.

4. MICROSCOPIC VISION/FORCE INTEGRATION CONTROL

4.1. Limitation of Microscopic Vision

Microscopic vision is essential to microassembly in providing non-contact feedback of microscale geometry, spatial relations, and motion. However, microscopic

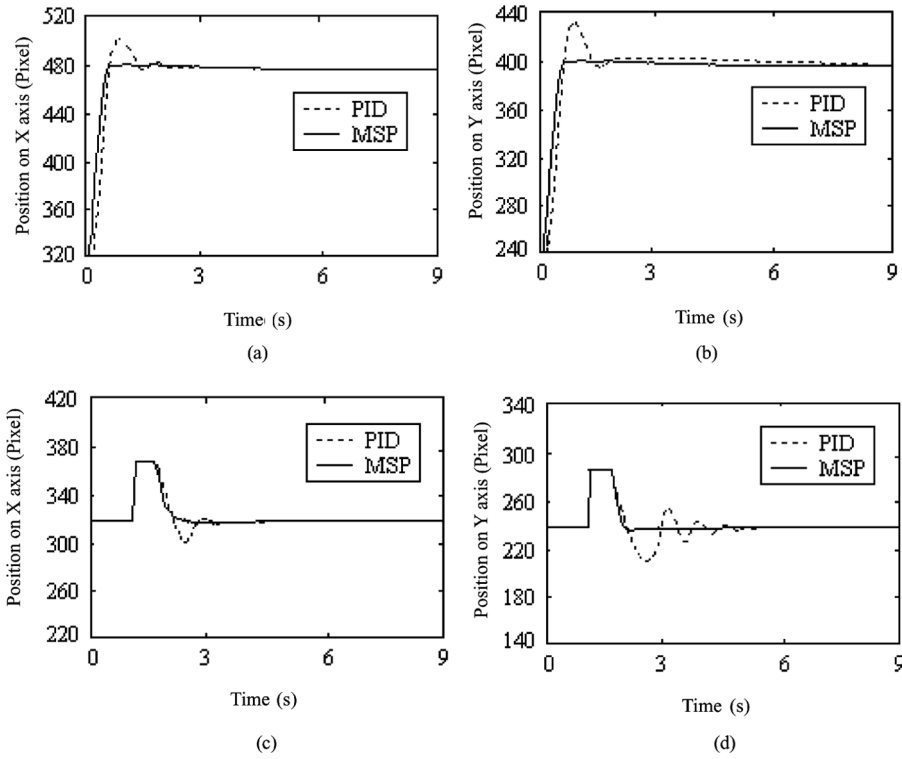


Figure 7. Comparisons of the single PID controller and the modified Smith predictor: (a) the point to point motion on the x axis; (b) the point to point motion on the y axis; (c) the disturbance rejection on the x axis; and (d) the disturbance rejection on the y axis.

vision has inherent limitations, such as time delay, easily disturbed by the circumstance and dependence on the calibration. In addition, physical interaction with the objects to be manipulated is essential. Therefore, sensing and control of interaction force between the microparts and environment, as well as the positioning performance, should be provided in the process of microassembly.

4.2. Integration Technique

In the assembly process, the 3-D PVDF force sensor is used for the gripping, transporting, preventing collision, and force sensing. A microscopic vision/force integration scheme is shown in Figure 8. A PID controller is used to control the contact force.

$$I_d = k_d \dot{y}_r + k_f (F_d - F_r) + k_I \int (F_d - F_r) dt \quad (15)$$

where F_d and F_r are the reference of force and force feedback, respectively. y_r and \dot{y}_r are the visual feedback of displacement and speed of micromanipulator, respectively. k_f , k_I and k_d are proportional, integral, and differential parameters, respectively. The control scheme that switches between visual servoing and force feedback control is

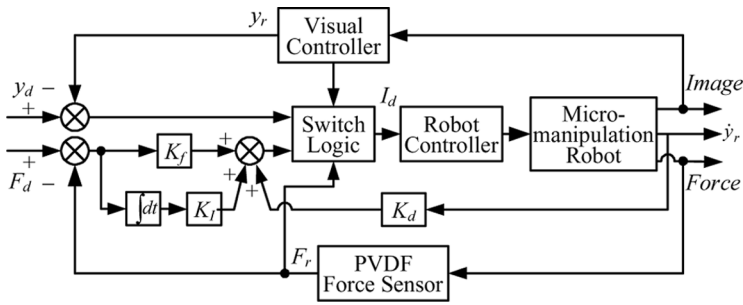


Figure 8. The microscopic vision/force integration scheme.

given by:

$$\text{If } \{ \{ \dot{y}_r(t_c) > 0 \cap F_r = F_c \} \cup \{ F_r < F_c \} \} \quad (16)$$

then switch to position control

$$\text{else } \{ \{ \dot{y}_r(t_c) \leq 0 \cap F_r = F_c \} \cup \{ F_r \geq F_c \} \} \quad (17)$$

then switch to force control

where $\dot{y}_r(t_c)$ is the speed of micromanipulator at time t_c . F_r and F_c are the contact force and force threshold, respectively.

5. EXPERIMENTS

5.1. Visual Positioning

The complex tasks which appear during the assembly have to be taken into consideration during the design and fabrication. In our experiment, the microparts fabricated by LIGA technology are arrayed on the wafer substrate. As Figure 2c shows, the planetary gears on the substrate have the same arrangement, and the direction A of one tooth is parallel to the y axis in the image frame. As Figure 2d shows, each annular wheel and sun gear have three marks on their surface. Three lines linking each two marks and the center of sun gear distribute symmetrically, and the angle between the adjacent lines is 120° . Midpoints O_1, O_2 , and O_3 between each two marks are the assembly points of planetary gears. The angle of the lines and the assembly points can be easily obtained by image processing and recognition, that is, the assembly point can be easily obtained. The positioning process under visual servoing is performed as follows:

- Recognize the marks on the sun gear and the annular wheel by image processing and image recognition. Then calculate the coordinates of midpoints O_1 , O_2 , and O_3 .
- Move one midpoint to the rotation center of the positioning stage. Then rotate the base frame to allow the line through the midpoint to be parallel with axis y in the image frame.
- Bring the planetary gear into the view of the microscope. Calculate its center coordinates by image processing. Then grasp the planetary gear and transport it to the base frame.
- Move down to the base frame. Adjust the planetary gear and the base frame to the coarse engaging state.

5.2. Fuzzy Logic Strategy for Engaging State Searching

During the searching phase of the planetary gear assembly task it is assumed that the end surface of the planetary gear does not completely lie within the engaging face. Hence, six contact configurations between the sun gear, planetary gear, and output wheel can be considered, three of which are illustrated in Figures 9a, 9b, and 9c. The remaining configurations are similar with the planetary gear rotated in the symmetrical position. The contact configurations can be examined by the contact force in the X - Y plane, which is parallel to the contact surface of the planetary gear.

The searching process on the y axis is illustrated in Figure 9d. The whole searching task is on the X - Y plane, keeping the contact force at a certain value on the z axis. The force threshold, F_0 is used to examine the contact force and simultaneously protect the micro-gears from becoming damaged. The threshold, D_0 , is confined as

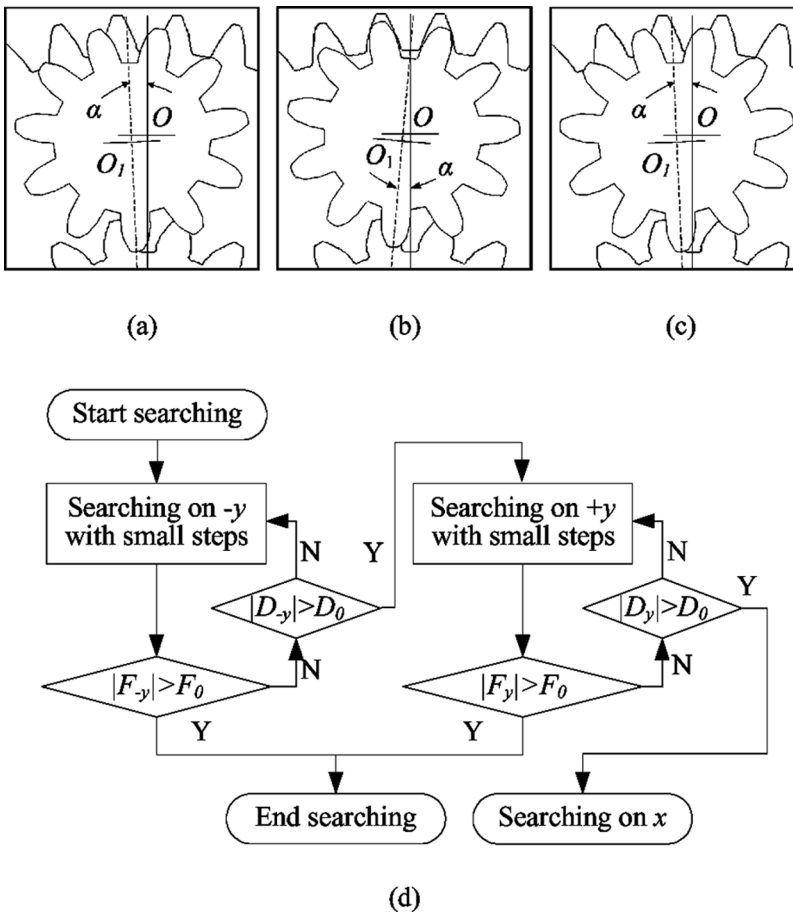


Figure 9. Strategy for engaging states searching: (a) the one-side contact configuration between the planetary gear and annular wheel; (b) the one-side contact configuration between the planetary gear and sun gear; (c) the two-side contact configuration with the sun gear and annular wheel; and (d) the searching process on the y axis.

the maximum displacement on the searching axes. All the thresholds are obtained from analyses and experiments. The searching process on the x axis is similar to the process on the y axis.

The contact configurations can be determined by the magnitude and direction of the contact force on the x axis and the y axis. The position and force curves in Figure 10 denote the contact configurations illustrated in Figure 9. The two-side

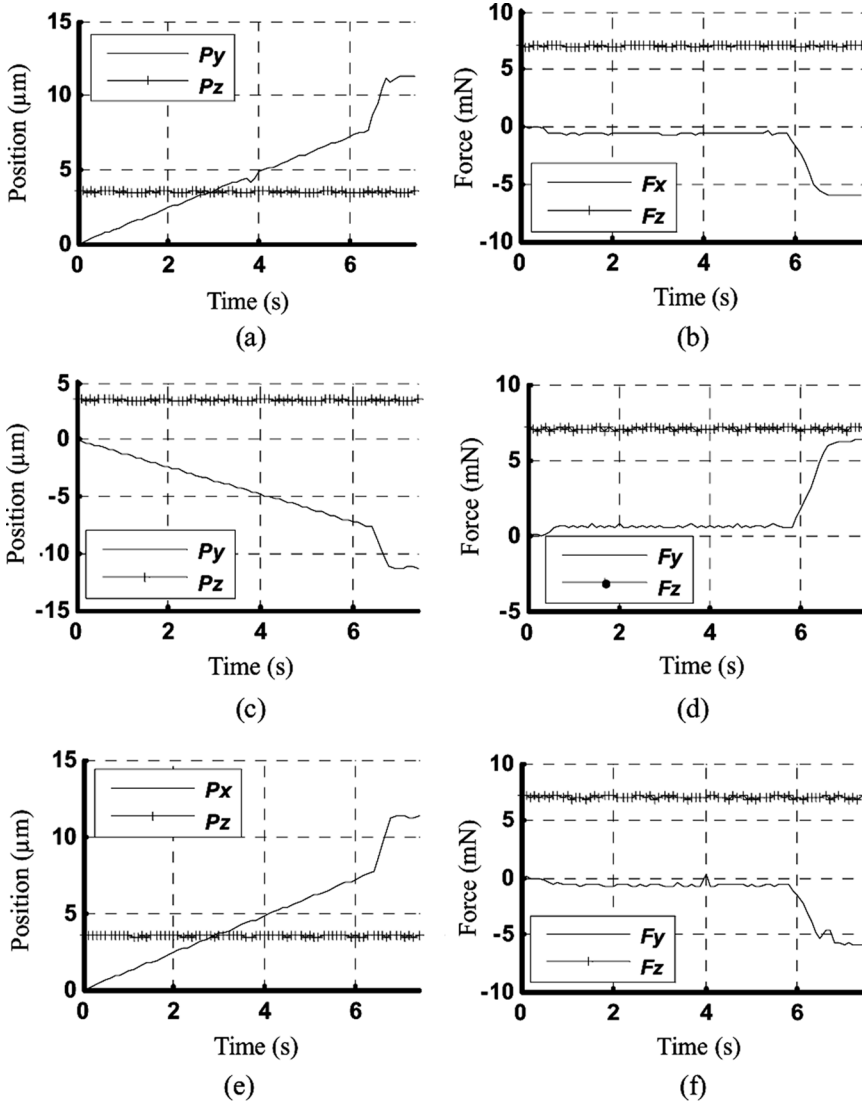


Figure 10. Curves of contact configurations. (a) and (b): the position and the force on the y axis and z axis of the one-side contact configuration between the planetary gear and the sun wheel; (c) and (d): the position and the force on the y axis and z axis of the one-side contact configuration between the planetary gear and the annular wheel; and (e) and (f): the position and the force on the y axis and z axis of the two-side contact configuration.

configuration can transform into the one-side configuration after the first searching. Then the engaging state can be obtained by the searching strategy of one-side configuration. When the configuration is examined, corresponding adjusting scheme with small steps is used to obtain the engaging state.

5.3. Tolerance Compensation Movement

The insertion phase is supported by the tolerance compensation movement and is illustrated in Figure 11, which represents a successful strategy of how to overcome the case of a jam or to avoid problems with the given minimal mounting gaps. The tolerance movement, including the translation and rotation, is driven by the 2-DOF and 3-DOF fine positioning stages mounted on the micromanipulator and positioning worktable, respectively.

According to the engaging principle, we can obtain

$$\begin{cases} \delta_{s1} = 2\pi r_j / z_1 - s_{j1} - s_{j2} \\ \delta_{t1} = a - (z_1 + z_2)m/2 - (x_1 + x_2)m, \end{cases} \quad (18)$$

$$\begin{cases} \delta_{s2} = 2\pi r_j / z_1 - s_{j2} - s_{j3} \\ \delta_{t2} = (z_2 + z_3)m/2 - (x_2 - x_3)m - a, \end{cases} \quad (19)$$

where δ_{1t} and δ_{1s} denote the addendum clearance and backlash between the sun gear and planetary gear, respectively. δ_{2t} and δ_{2s} denote the addendum clearance and backlash between the sun gear and planetary gear, respectively. r_j is the radius of the pitch circle of sun gear, a is the center to center spacing, and z_1 , z_2 , and z_3 are the tooth number of sun gear, planetary gear and annular wheel, respectively. s_{j1} , s_{j2} and s_{j3} are their corresponding tooth space and m is the modulus.

Then we can obtain the tolerances Δx and Δy on the x and the y axes,

$$-\delta_{t1} \leq \Delta y \leq \delta_{t2} \quad (20)$$

$$|\Delta x| \leq \min(\delta_{s1}, \delta_{s2}) \quad (21)$$

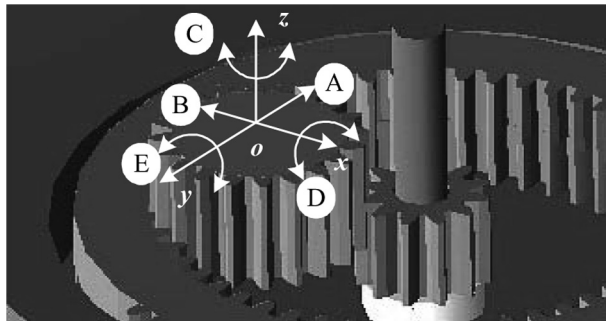


Figure 11. The tolerance compensation movement. A and B) the movement on y and x axes of positioning stages, respectively; C) oscillating rotation on x axis of positioning stage; D and E) oscillating rotation on x and y axes of micromanipulator, respectively.

Considering the inserting depth l which can be obtained by the liner encoder feedback, the tolerances α , β , and γ can be obtained.

$$|\alpha| \leq \arctan[\min(\delta_{s1}, \delta_{s2})/2(l_0 - l)] \quad (22)$$

$$|\beta| \leq \arctan[(\delta_{t1} + \delta_{t2})/(l_0 - l)] \quad (23)$$

$$|\gamma| \leq \arctan(\max(\delta_{s1}, \delta_{s2})/r_{j2}) \quad (24)$$

where l is the height of the annular wheel.

Hence, the tolerance on each axis for compensation movement is obtained. In order to improve the efficiency of the insertion task and to prevent microparts from being damaged, the adjustment range on each axis should be within the tolerance obtained above.

During the insertion phase, in order to overcome the assembly resistance, the force on the z axis is about 16 mN, which is usually more than the force on the z axis during the searching phase. Forces on the z axis are illustrated in Figure 12. The accomplishment of the assembly task can be examined by the force on the z axis when it exceeds the force threshold, which is obtained by experiments. In our experiment, the threshold is 36 mN and the insertion velocity on the z axis is 40 $\mu\text{m/s}$. The total insertion depth is about 250 μm .

During the entire experiment, human intervention is used to aid the grasping of annual gears, and then the microscopic vision/force integration was used to assemble three planetary gears into the base frame which is fixed with a sun gear and an annular wheel. Fifty assembly experiments were carried out to evaluate the system capability; 43 assembly experiments have been completed. Failure took place during the vision positioning process because of the blurry marks. In the experiments, there was no case of jamming during the inserting process, mainly because of the large gap between the gears, which is near 3 μm . Each planetary gear can be assembled within 90 seconds and three of them took the minimum time, which is about 80 seconds. The assembly result is shown in Figure 13.

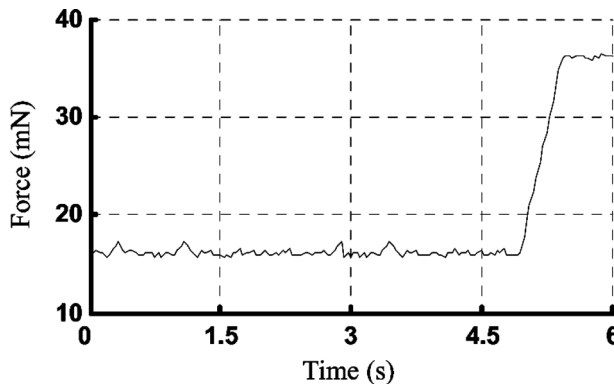


Figure 12. Force curves on z axis in the inserting phase.

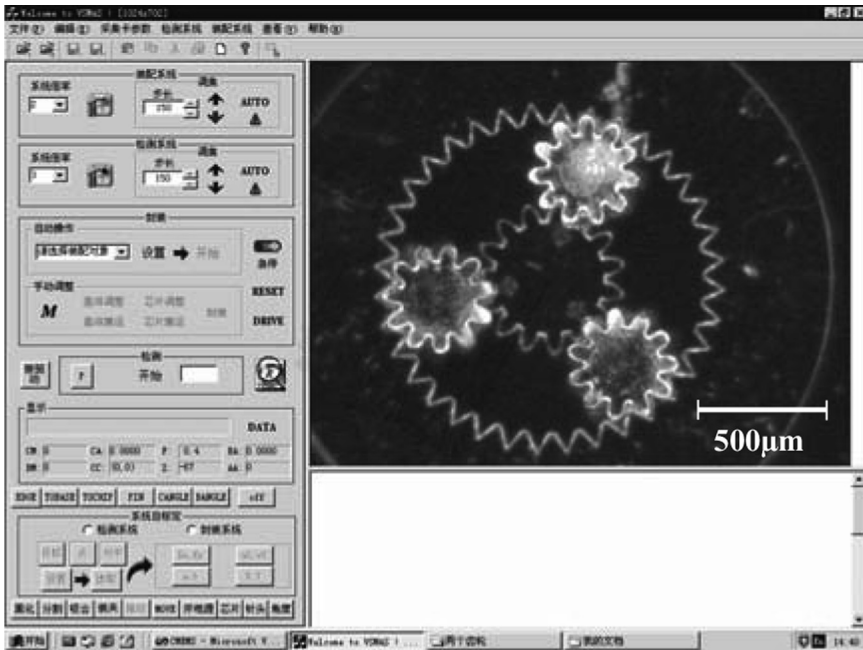


Figure 13. The assembly result.

6. CONCLUSION

Flexible microassembly systems are an important trend in the design and development of systems with the characteristics of versatility, flexibility, and robustness to achieve small and medium-sized batches assembled in an economical way. To increase the variations in system configuration, the system components, including positioning stages, micromanipulator, gripper, vision system, control system, and auxiliary systems, should be built with a modular architecture. Regarding the limitation of existing microscopic vision, microscopic vision/force integration techniques can be used to achieve high-precision and stable microassembly. The successful microassembly of three planetary gears has been presented to illustrate and validate the performance and adaptability of the developed system. Much research remains to be accomplished in improving the reliability and capacity of microassembly systems in implementing high-precision microgrippers and multiple DOF microscale force sensors with the characteristics of versatility and flexibility. Research is also needed in the kinematic and dynamic modeling of micromanipulation and in developing robust control strategies.

REFERENCES

- Bi, Z. M., W. A. Gruver, and W. J. Zhang. 2003. Adaptability of reconfigurable robotic system. *Proc. IEEE Int. Conf. on Robotics and Automation* 2:2317–2322.
- Eberhardt, R., T. Schellar, G. Tittelbach, and V. Guyenot. 1998. Automated assembly of micro-optical components. *Proc. SPIE Microrobotics and Microsystem Fabrication* 3202:117–127.

- Firestone, Lawrence, Kitty Cook, Kevin Culp, Neil Talsania, and Kendall Preston Jr. 1991. Comparison of autofocus methods for automated microscopy. *Cytometry* 12:195–206.
- Groen, F., I. T. Young, and G. Lighthart. 1985. A comparison of different focus functions for use in autofocus algorithms. *Cytometry* 6:81–91.
- Kim, Byungkyu, Hyunjae Kang, Deok-Ho kim, Gwi Tae Park, and Jong-Oh Park. 2003. Flexible microassembly system based on hybrid manipulation scheme. *Proc. IEEE Conf. on Intelligent Robots and System* 2:2061–2066.
- Lee, Woo Ho and Byoung Hun Kang. 2003. Micropeg manipulation with a compliant micro-gripper. *Proc. IEEE Int. Conf. on Robotics and Automation* 3:3213–3218.
- Liu, Pinkuan, Lining Sun, Dongsheng Qu, and Weibin Rong. 2002. Dynamic analysis on a novel nanopositioning stage driven by PZT. *Optics and Precision Engineering* 10:143–147.
- Liu, Yanfei, Adam W. Hoover, and Ian D. Walker. 2004. A timing model for vision-based control of industrial robot manipulators. *IEEE Trans. on Robotics* 20:891–898.
- Maeda, Yusuke, Haruka Kikuchi, and Hidemitsu Izawa. 2003. An easily reconfigurable robotic system. *Proc. IEEE Int. Conf. on Robotics and Automation* 2:2586–2591.
- Mallat, S. 1999. *A wavelet tour of signal processing*, 2nd ed. Boston: Academic Press.
- Popa, Dan, Byoung Hun Kang, Jeongsik Sin, and Jie Zou. 2002. Reconfigurable micro-assembly system for photonics application. *Proc. IEEE Int. Conf. Robotics Automation* 2:1495–1500.
- Qu, Dongsheng, Lining Sun, Jianguo Wang, and Chang Qin. 2002. Study on precision nanopositioning system based on piezo-actuator. *Piezoelectrics & Acoustooptics* 24:506–509.
- Ralis, Stephen J., Barmeshwar Vikramaditya, and Bradley J. Nelson. 2000. Micropositioning of a weakly calibrated microassembly system using coarse-to-fine visual servoing strategies. *IEEE Trans. Elec. Pack. Manu.* 23:123–131.
- Santa, Karoly, Sergej Fatikow, and Gabor Felso. 1999. Control of microassembly-robots by using fuzzy-logic and neural network. *Comp. Industry* 39:219–227.
- Santos, A., C. Ortiz De Solorzano, J. J. Vaquero, J. M. Pena, and F. Del Pozo. 1997. Evaluation of autofocus functions in molecular cytogenetic analysis. *J Microscopy* 188:264–272.
- Subbarao Murali, Tae Choi, and Arman Nikzad. 1993. Focusing techniques. *Optical Engineering* 32:2824–2836.
- Subbarao Murali and Jenn Kwei Tyan. 1998. Selecting the optimal focus measure for autofocusing and depth-from-focus. *IEEE Trans. Pattern Analysis and Machine Intelligence* 20:864–870.
- Sugi, Masao, Yusuke Maeda, Yasumichi Aiyama, Tomokazu Harada, and Tamio Aral. 2003. A holonic architecture for easy reconfiguration of robotic assembly systems. *IEEE Trans. on Robotics and Automation* 19:457–464.
- Sun, Lining, Hui Xie, Weibin Rong, and Liguog Cheng. 2005. Task-reconfigurable system for MEMS assembly. *Proc. IEEE Int. Conf. on Robotics and Automation* 844–849.
- Sun, Yu, Stefan Duthaler, and Bradley J. Nelson. 2004. Autofocusing in computer microscopy: selecting the optimal focus algorithm. *Microscopic Research and Techniques* 65:139–149.
- Vikramaditya, Barmeshwar. 2001. Micromanipulation using self assembly strategies. PhD diss., University of Minnesota.
- Vikramaditya, Barmeshwar and Bradley J. Nelson. 1997. Visually guided microassembly using optical microscopes and active vision techniques. *Proc. IEEE Int. Conf. on Robotics and Automation* 4:3172–3177.
- Vincze, Markus. 2000. Dynamics and system performance of visual servoing. *Proc. IEEE Int. Conf. on Robotics and Automation* 1:644–649.

- Woern, H., J. Seyfried, S. Fahlbusch, A. Buerkle, and F. Schmoeckel. 2000. Flexible microrobots for micro assembly tasks. *IEEE Symposium on Micromechanics and Human Science* 135–143.
- Xie, Hui, Liguang Cheng, Weibin Rong, and Lining Sun. 2005. Hybrid vision-force control for miniaturized gear system assembly. *Proc. IEEE Int. Conf. on Robotics and Automation* 1380–1385.
- Yang, Ge and Bradley J. Nelson. 2003. Wavelet-based autofocusing and unsupervised segmentation of microscopic image. *Proc. IEEE Int. Conf. on Intelligent Robots and System* 3:2143–2148.
- Yang, Ge, J. A. Gaines, and B. J. Nelson. 2005. Optomechatronic design of microassembly systems for manufacturing hybrid Microsystems. *IEEE Trans. on Industrial Electronics* 52:1013–1023.
- Zhai, Baonian, Siak-Piang Lim, Kwok-Hong Lee, Shuxiang Dong, and Pin Lu. 2000. A modified ultrasonic linear motor. *Sensors and Actuators A – Physics* 86:154–158.
- Zhou, Yu, Badley J. Nelson, and Barmeshwar Vikramaditya. 1998. Fusing force and vision feedback for micromanipulation. *Proc. IEEE Conf. on Robotics and Automation* 2:1220–1225.